Comparison of the ultimate direction-finding capabilities of a number of planar array geometries

A. Manikas Ph.D., DIC, AMIEE, MIEEE*

A. Alexiou Dip. EE*

H. R. Karimi Ph.D., DIC, AMIEE+

Department of Electrical and Electronic Engineering,

Imperial College of Science, Technology and Medicine,

London, SW7 2BT

***short title**: Ultimate DF capabilities of planar arrays*

ABSTRACT

Although the properties of Direction-Finding (DF) algorithms have been investigated extensively, the fundamental effects of the array configuration on the performance of DF systems remain unknown. Furthermore it is often overlooked that there are some theoretical lower limits on the DF performance which are imposed by the array geometry itself. In this paper eight diverse array geometries of elevated feed monopoles, which are used in a number of experimental sites in the UK, are investigated and compared using the ultimate detection, resolution and accuracy thresholds as figures of merit.

*A. Manikas and A. Alexiou are with the Department of Electrical and Electronic Engineering, Imperial College of Science, Technology and Medicine, Exhibition Road, London SW7 2BT, UK.

+H. R. Karimi was formely with Imperial College of Science, Technology and Medicine and is now with Motorola, GSM Products Division, 16 Euroway, Blagrove, Swindon, Wiltshire, SN5 8YQ.

NOTATION

A, a	scalar
$\underline{A}\,, \underline{a}$	vector
$\mathbb{A}\,, \underline{\underline{\mathbf{A}}}$	matrix
$(.)^{\mathrm{T}}$	transpose
$(.)^{\mathrm{H}}$	conjugate transpose
$\underline{a}^2$	element by element square
$\lvert a \rvert$	absolute value of a scalar
$\lvert\, \underline{a}\, \rvert$	Euclidian norm of vector
$\mathbb{P}$	projection operator
$\mathbb{P}^{\perp}$	orthogonal projection operator
$\mathcal{R}^N$	real N-dimensional space
$\mathcal{C}^N$	complex N-dimensional space
p	general bearing parameter
θ	azimuth bearing
ϕ	elevation bearing
s	arc length parameter
$\dot{s}(p)$	rate of change of arc length of p-curve
Δp	bearing separation $\lvert p_1 - p_2 \rvert$
Δs	arc length separation $\lvert s_1 - s_2 \rvert$
$\dot{a}$	$\partial a / \partial p$
a'	$\partial a / \partial s$
κ_i	i-th curvature
N	number of sensors
M	number of sources
L	number of snapshots (observation interval)
P	signal power
σ^2	noise power
$\exp\{\mathbb{A}\}$	element by element exponential
$\mathrm{sum}(\underline{a})$	sum of the elements of vector $\underline{a}$
$\mathcal{L}\{\underline{a}\,, \underline{b}\}$	subspace spanned by vectors $\underline{a}$ and $\underline{b}$
DF	Direction Finding
DOA	Direction Of Arrival
CRB	Cramér-Rao Bound
SNR	Signal-to-Noise Ratio
RMS	Root-Mean Square

1. INTRODUCTION

Consider a planar array of N sensors receiving M narrow-band plane waves. The response of the array to a signal incident from azimuth $\theta \in [0, 360^\circ]$ and elevation $\phi \in [0, 90^\circ]$ is described by the *source position vector* (or manifold vector) which is defined as

$$\underline{a}(\theta,\phi) = \exp\{ -j\, \underline{\underline{\mathbf{r}}}\, \underline{k}(\theta,\phi)\} = \exp\Big\{ -j\,\pi\, (\underline{r}_{\mathrm{x}}\cos\theta + \underline{r}_{\mathrm{y}}\sin\theta)\, \cos\phi \Big\} \tag{1}$$

where $\underline{\underline{\mathbf{r}}} = [\,\underline{r}_{\mathrm{x}},\ \ \underline{r}_{\mathrm{y}},\ \ \underline{r}_{\mathrm{z}}\,] \in \mathcal{R}^{N\times 3}$ is the matrix of sensor locations (in units of half-wavelengths) and $\underline{k}(\theta,\phi) = \pi[\,\cos\theta\cos\phi,\ \ \sin\theta\cos\phi,\ \ \sin\phi\,]^{\mathrm{T}} \in \mathcal{R}^{3\times 1}$ denotes the wavenumber vector. The array manifold is then defined as the locus of the vector $\underline{a}(\theta,\phi)\ \ \forall\theta,\phi$.

The overall performance of a DF system is a function of both the array geometry/characteristics and the DF algorithm employed, since a particular algorithm behaves differently when used in conjunction with different array structures and, similarly, a certain array generates different results when its output is applied to different algorithms.

The effect of the array structure on the system performance may be assessed quantitatively by determining the *shape* and *orientation* of the array manifold through the study of the manifold's differential geometry [1,2,3,4]. In the case of a linear array employed in a θ direction-finding system (where $\phi = 0$ and $\underline{r}_{\mathrm{y}} = \underline{r}_{\mathrm{z}} = \underline{0}$) the array manifold is a single curve shaped in the form of a **hyperhelix**[1] [1] and, therefore, can be fully characterised by its length and curvatures. However, in a (θ, ϕ) direction-finding system which employs a planar array, the manifold is a two-parameter surface lying on a hypersphere of radius $\sqrt{N}$ embedded in $\mathcal{C}^N$ and is shaped in the form of a conoid. The parameters of this conoid have been estimated in [2]. Alternatively

[1] A **hyperhelix** is a curve whose curvatures remain constant at all points along its length.

the surface of this conoid can be considered to consist of two families of constant-parameter curves defined as follows

$$\begin{cases} \theta\text{-parameter curves } \underline{a}(\theta\,|\phi_i) & (\theta\text{-curves of constant elevation } \phi_i) \\ \phi\text{-parameter curves } \underline{a}(\phi\,|\theta_i) & (\phi\text{-curves of constant azimuth } \theta_i) \end{cases}$$

where each family can be used to fully describe the array manifold surface. The properties of these curves have been investigated in [3] and are summarised next.

ϕ-parameter curves

According to Equation (1), the manifold surface of a planar array can be generated by a family of ϕ-parameter curves which meet at the apex of the manifold for $\phi = 90^\circ$ and can be described as

$$\underline{a}(\phi) = \exp\Big\{ -\, j\pi\, \underline{R}(\theta)\, \cos\phi \Big\} \qquad \text{with} \qquad \theta\text{=constant} \tag{2}$$

$$\text{where} \quad \underline{R}(\theta) = \underline{r}_{\mathrm{x}}\cos\theta + \underline{r}_{\mathrm{y}}\sin\theta.$$

Equation (2) can be seen as the manifold of an equivalent linear array with sensor locations given by the vector $\underline{R}(\theta)$. This implies that the ϕ-parameter curves of a planar array are shaped as complex hyperhelices [1,3].

θ-parameter curves

The manifold surface can also be generated by a family of θ-parameter curves

$$\underline{a}(\theta) = \exp\Big\{ -\, j\pi\, \underline{R}(\theta)\, \cos\phi \Big\} \qquad\qquad \phi\text{=constant} \tag{3}$$

These curves are not **hyperhelical** and only limited information, regarding their complete shape, is available. A hyperhelical curve $\underline{a}(p)$ such as a ϕ-curve is analytically 'convenient' in the sense that all its curvatures are independent of the parameter p, hence the procedure for their calculation is identical to that of linear arrays [1]. However, for a non-helical curve, such as a θ-curve, this is not the case and an analytical approach for the calculation of all curvatures is impractical. Fortunately, the first curvature is quite adequate for describing a curve's shape at a local level.

The essential properties of both θ and ϕ curves, which will be used in this study, are:

- the **arc length** s, (the most basic feature of a curve)

$$s(p) = \int_{p_{\mathrm{o}}}^{p} \left| \frac{\mathrm{d}\underline{a}(p)}{\mathrm{d}p} \right| \mathrm{d}p \tag{4}$$

- the **rate of change of arc length** $\dot{s}$:

$$\dot{s}(p) = \frac{\mathrm{d}s}{\mathrm{d}p} = |\dot{\underline{a}}(p)| \tag{5}$$

- and the first curvature $\kappa_1(p)$

where p is a generic parameter representing both θ and ϕ.

Table 1 provides analytical expressions for the first curvature and the rate of change of arc length of both θ and ϕ curves for a planar array. Note that the differential geometry of the θ-curves varies as a function of azimuth with a periodicity of at least 180°.

Table 1: Differential geometry features of planar array manifold		
parameter curves	**ϕ- curves**	**θ- curves**
rate of change of arc length	$\dot{s}(\phi) = \pi \sin\phi \, \lvert\underline{R}\rvert$	$\dot{s}(\theta) = \pi \cos\phi \, \lvert\underline{R}_\theta\rvert$
first curvature	$\kappa_1(\phi) = \lvert\widetilde{\underline{R}}^{\,2}\rvert$	$\kappa_1(\theta) = \frac{1}{\lvert\underline{R}_\theta\rvert^2} \left\lvert \underline{R}_\theta^2 + \frac{\mathrm{j}}{\pi\cos\phi} \mathbb{P}^{\perp}_{\underline{R}_\theta} \underline{R} \right\rvert \simeq \lvert\widetilde{\underline{R}}^{\,2}_{\theta}\rvert$
where $\underline{R} = \underline{r}_x\cos\theta + \underline{r}_y\sin\theta$, $\widetilde{\underline{R}} = \frac{\underline{R}}{\lvert\underline{R}\rvert}$, $\underline{R}_\theta = \frac{\partial \underline{R}}{\partial\theta}$, $\widetilde{\underline{R}}_\theta = \frac{\underline{R}_\theta}{\lvert\underline{R}_\theta\rvert}$		

In this paper eight array geometries are compared according to three fundamental limits which are imposed on the performance of a superresolution DF system by the **array structure** employed. These are

- the detection threshold
- the resolution threshold
- the estimation accuracy lower bound

where each is a function of the differential geometry of manifold parameter curves.

These limits will be used as *figures of merit* for the different array structures. Since no DF algorithm can exceed these performance levels they also provide a benchmark against which any DF algorithm can be compared.

The outline of the paper is as follows:

In Section 2 the detection, resolution and accuracy limits which specify the ultimate performance provided by a direction-finding system, are introduced as *figures of merit*, under the assumptions of a finite number of snapshots and a finite signal-to-noise ratio.

In Section 3 eight diverse planar array geometries of elevated feed monopoles (used in a number of experimental sites in the UK) are presented, while in Section 4 these array geometries are compared and their relative merits are determined according to the criteria established in Section 2. In Section 5 the comparison is performed with the array geometries normalised with respect to aperture and number of sensors. Finally, in Section 6 the paper is concluded.

2. PERFORMANCE CRITERIA

The most essential feature of signal subspace type techniques is their ability to eliminate the effects of noise from the estimation process and thus to provide exact estimates of the signal subspace spanned by the true manifold vectors. This feature is achieved asymptotically over an infinite number of snapshots (the observation interval). Unfortunately in practice the availability of only a limited number of snapshots, L, prevents the full elimination of the noise and can result in poor direction finding performance. This 'uncertainty' due to the remaining noise has been modelled in [4] based on the processing of L snapshots at the output of an N-element array which receives M signals in the presence of noise of power σ^2. The conclusion of the investigation in [4] is that the 'uncertainty' due to the remaining noise in the estimation process of the i-th signal after L snapshots can be represented as an N-dimensional hypersphere centered at the point $\underline{a}_i$ whose radius σ_{e_i} represents the RMS value of the remaining noise. These spheres are known as *uncertainty spheres* and they 'shrink' as a function of the observation interval according to the model

$$\sigma_{e_i}=\sqrt{\frac{\sigma^2}{2L\,P_i\,C}} \qquad i=1,...M$$

where P_i denotes the power of the i-th source. The factor C is a positive real number smaller than or equal to 1 (i.e. $0<C\leq 1$) which models the additional uncertainties introduced by the employment of a specific practical DF algorithm. The value $C=1$ corresponds to a theoretical limit achieved by an 'ideal' DF-algorithm which does not introduce extra uncertainties and eliminates any dependency which may exist between the received signals (for instance decorrelating any correlated signals, etc).

Consider the case of two closely spaced emitters with manifold vectors $\underline{a}_1$ and $\underline{a}_2$. The thresholds of detection and resolution can be identified in terms of the relative positions of the *uncertainty spheres* centered at points $\underline{a}_1$ and $\underline{a}_2$. Then, according to [4],

"Two sources are detected if and only if the uncertainty spheres do not make contact"

with the implication that the *detection threshold* occurs when the two uncertainty spheres *just make contact*. It should be emphasised that detecting the presence of two sources does not necessarily mean that their bearings have been resolved. In fact for a sufficiently low SNR or a sufficiently small number of snapshots, a typical high-resolution algorithm will always provide a spectrum with a single null, even if it has been given the true number of sources a priori.

If a similar line of arguments is followed for the resolution then

> " ***Two sources corresponding to points*** s_1 ***and*** s_2 ***on the manifold are resolved if and only if the uncertainty spheres do not make contact with the subspace*** $\mathbb{H} = \mathcal{L}\{\underline{a}(s_0), \underline{u}_1(s_0)\}$ ***at any point*** s_0 **between** s_1 ***and*** s_2 ***where*** $\underline{u}_1 = \dfrac{d\underline{a}(s_o)}{ds}$."

and, in this case, the *resolution threshold* occurs when the uncertainty spheres *just make contact* with the worst case signal subspace $\mathbb{H}$.

According to the model of uncertainty spheres and the above definitions of *detection* and *resolution thresholds*, the products $(\text{SNR}_1 \times L)$ required for a source of power P_1 to be detected and resolved in the presence of a source of power P_2, when the two sources have a bearing separation Δp, are respectively

$$(\text{SNR}_1 \times L)_{det} = \frac{1}{2\, C(\Delta p \times \dot{s}(p))^2} \left(1 + \sqrt{\frac{P_1}{P_2}}\right)^2 \tag{6}$$

and

$$(\text{SNR}_1 \times L)_{res} = \frac{2}{C\,(\Delta p \times \dot{s}(p))^4 \left(\widehat{\kappa}_1^2(p) - \frac{1}{N}\right)} \left(1 + \sqrt[4]{\frac{P_1}{P_2}}\right)^4 \tag{7}$$

where[2]

$$\widehat{\kappa}_1(p) = \begin{cases} \sqrt{\kappa_1^2(\phi) - \text{sum}^2(\widetilde{\underline{R}}^{\,3})} & \text{when} \quad p = \phi \\ \sqrt{\kappa_1^2(\theta) - \text{sum}^2(\widetilde{\underline{R}}_{\theta}^{\,3})} & \text{when} \quad p = \theta \end{cases} \tag{8}$$

and p is a parameter representing ϕ or θ. In the above expressions it is assumed that the reference point is taken at the array centroid. Bearing p corresponds to arc length $(s_1 + s_2)/2$ on the manifold, which, to a first order approximation, also corresponds to bearing $(p_1 + p_2)/2$. Note also that the arc length separation is related to the bearing separation with the expression $\Delta s = \Delta p \times \dot{s}(p)$. For $C = 1$ the above expressions become 'lower bounds' and form a benchmark against which any practical DF algorithm can be compared.

Having presented the detection and resolution criteria, the discussion will be confined to the estimation accuracy. The estimation accuracy can be expressed in terms of the error variance of the estimation of the parameter p_1 for a source of power P_1 in the presence of a source of power P_2. If the two sources have a bearing separation Δp, then this estimation accuracy is bounded by the Cramér-Rao Bound [3,5]

$$\text{CRB}[p_1] = \frac{1}{2\text{SNR}_1 \times L} \left(\dot{\underline{a}}_1^{\text{H}}\, \mathbb{P}_{\mathbb{A}}^{\perp}\, \dot{\underline{a}}_1\right)^{-1} \simeq \frac{1}{\text{SNR}_1 \times L} \frac{2}{(\Delta p \times \dot{s}(p))^2\, \dot{s}^2(p_1)\, \left(\widehat{\kappa}_1^2(p) - 1/N\right)} \tag{9}$$

[2] $\widehat{\kappa}_1$ is the first curvature of the circular approximation to the manifold, i.e. it takes into account the orientation of the manifold in the N-dimensional observation space.

where $\underline{a}_1$ is the source position vector corresponding to the source at p_1 and SNR_1 is the signal-to-noise ratio of the signal impinging from bearing p_1.

Furthermore, if the CRB is evaluated at the threshold level $(\text{SNR}_1 \times L)_{res}$, then the estimation error (accuracy of the estimate) at the resolution threshold is given as follows:

$$\text{CRB}[p_1]_{res} = \frac{1}{2(\text{SNR}_1 \times L)_{res}} \left(\dot{\underline{a}}_1^{\text{H}} \, \mathbb{P}_{\mathbb{A}}^{\perp} \, \dot{\underline{a}}_1 \right)^{-1} \simeq \frac{C}{\left(1+\sqrt[4]{\frac{P_1}{P_2}}\right)^4} \, \frac{(\Delta p \times \dot{\text{s}}(p))^2}{\dot{\text{s}}^2(p_1)}$$

It is important to note that for two equi-powered sources the above expression is simplified (for $C = 1$) to

$$(\text{ RMS } \textit{estimation error at resolution threshold}) \geq \sqrt{\text{CRB}[p_1]_{res}} \simeq \frac{\Delta p}{4} \cdot \frac{\dot{\text{s}}(p)}{\dot{\text{s}}(p_1)} \quad \rightarrow \quad \frac{\Delta p}{4}$$

which is an expected result indicating the generality and significance of the resolution threshold.

The above discussion was carried out under the assumption that the planar array consists of antennas that are isotropic (with gain of unity) in both azimuth θ and elevation ϕ. This assumption might seem unrealistic since many practical antennas (like the elevated-feed monopoles which will be investigated in this study) are non-isotropic and exhibit a complex gain response $g \in \mathcal{C}^1$ as a function of one or both bearing parameters. In this case the array manifold is given by

$$\underline{a}_g(\theta, \phi) = g(\theta, \phi) \underline{a}(\theta, \phi) \tag{10}$$

By using $\underline{a}_g(p)$ instead of $\underline{a}(p)$, where $p = (\theta, \phi)$, Equations (6), (7) and (9) can be transformed for directional sensors to the expressions presented in Table 2. It is clear from Table 2 that the directional pattern $g(p)$ of a directional sensor behaves simply as a "voltage gain" term boosting or deteriorating the effective Signal-to-Noise ratio at the output of the array. Consequently, it can be stated that the presence of directional sensors **does not** affect the relative merits of one array geometry over the other, although of course, performance is affected in absolute terms.

Table 2: DF capabilities criteria for directional arrays
$\text{CRB}[p_1] = \frac{1}{2\ \text{SNR}_1 \times L\ \lvert g(p_1)\rvert^2} \left(\dot{\underline{a}}_1^{\text{H}} \, \mathbb{P}_{\mathbb{A}}^{\perp} \, \dot{\underline{a}}_1 \right)^{-1} \simeq \frac{1}{\text{SNR}_1 \times L\ \lvert g(p_1)\rvert^2} \ \frac{2}{(\Delta s)^2\ \dot{\text{s}}^2(p_1)\ \left(\widehat{\kappa}_1^2(p) - 1/N\right)}$
$(\text{SNR}_1 \times L)_{det} = \frac{1}{2(\Delta p \times \dot{\text{s}}(p))^2 \lvert g(p_1)\rvert^2} \left(1 + \sqrt{\frac{\lvert g(p_1)\rvert^2 P_1}{\lvert g(p_2)\rvert^2 P_2}} \right)^2$
$(\text{SNR}_1 \times L)_{res} = \frac{2}{(\Delta p \times \dot{\text{s}}(p))^4 \left(\widehat{\kappa}_1^2(p) - \frac{1}{N} \right) \lvert g(p_1)\rvert^2} \left(1 + \left(\frac{\lvert g(p_1)\rvert^2 P_1}{\lvert g(p_2)\rvert^2 P_2} \right)^{1/4} \right)^4$

Performance as a function of elevation

Manifold differential geometry reveals that the variation of array performance with elevation ϕ is independent of array geometry and consequently the merits of one array configuration as compared with another remain unaltered at different elevations, i.e. performance comparison need only be carried out at a single elevation ϕ_o. The choice of ϕ_o is arbitrary and can be made according to the particular application. Here we consider an elevation of ϕ_o=30° at which the elevated feed monopoles, which will be used in this study, exhibit maximum gain.

Another characteristic feature of planar arrays of isotropic sensors is that while azimuth-estimation performance is greatest at low elevations, elevation-estimation performance is greatest at high elevations. Naturally this characteristic is masked by the directional pattern of the array elements.

Performance as a function of azimuth

Manifold differential geometry also reveals that the ϕ- and θ-estimation capabilities of a planar array are dependent on azimuth θ through vector $\underline{R}(\theta)$ and its derivative $\underline{R}_\theta(\theta) = \underline{R}(\theta + 90°)$ respectively. $\underline{R}(\theta)$ and $\underline{R}_\theta(\theta)$ are both direct functions of the array configuration and are 90° out of phase.

It is evident from Equations (6), (7) and (9), that **an array is a more powerful direction finder along those azimuths θ which correspond to larger values of $|\underline{R}(\theta)|$ (for ϕ-estimation) and larger values of $|\underline{R}(\theta + 90°)|$ (for θ-estimation)**, where $\underline{R}(\theta)$ equals the sensor locations when the array is projected along the azimuthal direction θ (Figure 1). This rule is particularly easy to apply in cases where the sensors are predominantly distributed along one direction. In such cases it is easy to judge the variations of $|\underline{R}(\theta)|$ with θ, by a simple observation of the array geometry. For more complicated array structures the variations of $|\underline{R}(\theta)|$ are not so obvious and actual computation is necessary. In the following section the variations of performance with azimuth will be examined in detail for a number of different array configurations.

3. ARRAY GEOMETRIES FOR STUDY

The eight array geometries investigated in this paper consist of vertical elevated-feed monopoles which are directional in elevation but isotropic in azimuth. These array structures are used in a number of experimental sites in the UK operating as DF systems in the HF frequency band (3 to 30 MHz) and employ monopoles of 12 meters height. Figure 2 shows the elevation gain pattern of these monopole-antennas. The pattern consists

of a single beam pointing at an elevation of approximately $\phi = 30^\circ$ with nulls at $\phi = 90^\circ$ (due to the vertical orientation of the monopole) and $\phi = 0^\circ$ (due to the reflectivity of conducting ground). Such antennas are unsuitable for the reception of ground-waves or high elevation signals but are often employed in the over-the-horizon reception of long-range sky-waves.

The eight array geometries, which will be investigated, are

- a linear array of 20 antennas (sensors) consisting of monopoles uniformly spaced at 27.58m, with the exception of the end-sensors which are at double spacing;
- a 24-element uniform circular array of 75m radius;
- Y, X, L and $\vdash$ (CROSS) shaped arrays with each branch of these shapes having 8 monopoles with locations [8m, 22m, 38m, 57m, 79m, 105m, 136m, 170m];
- two 8-element arrays with dual-ring and dual-spiral geometries respectively.

Figure 3 illustrates the above described array geometries, in meters. Note that the array centroids are used as the reference point (0m,0m).

Finally, we have seen in Section 2 that the variations in θ-estimation performance and ϕ-estimation performance, as a function of θ, are essentially identical apart from a phase of 90° (due to dependence on $|\underline{R}(\theta + 90°)|$ and $|\underline{R}(\theta)|$ respectively) and a scaling factor (due to dependence on cosϕ and sinϕ respectively). Therefore, only the θ-estimation performances for ϕ_o=30° will be investigated and compared in the following section. Various array geometries and values of θ from 0° to 180° are considered, while the results are repeated for θ from 180° to 360°.

4. COMPARISON BASED ON DETECTION, RESOLUTION AND ACCURACY CRITERIA

The theoretical lower limits on the accuracy, detection and resolution thresholds imposed on a DF system by the array geometry itself were evaluated for the array geometries described in the previous section. The results are presented in Figures 4-6 for an operating frequency of 15MHz. A discussion associated with the performance of each geometry is presented below.

Linear Array

The behaviour of a linear array can be readily predicted by noting that $\underline{R}(\theta) = \underline{r}_x \cos\theta$ and that $\underline{R}_\theta(\theta) = \underline{R}(\theta+90°) = -\underline{r}_x \sin\theta$. Hence one could predict that a linear array would have great difficulty in estimating azimuth bearings near 0° or 180° (end-fire) where $|\underline{R}(\theta)| = 0$. This is demonstrated in Figures 4-6, where the three criteria $(\text{SNR} \times L)_{det,\theta}$, $(\text{SNR} \times L)_{res,\theta}$ and CRB_θ tend to infinity at the above angles.

One could also predict that a linear array would have highest azimuth estimation capability for azimuths near 90° (broadside) where $|\underline{\text{R}}(\theta)|$ is maximum. Again this is confirmed in Figures 4-6 where the functions $(\text{SNR} \times L)_{det,\theta}$, $(\text{SNR} \times L)_{res,\theta}$ and CRB_θ are smallest at θ=90°.

Circular Array

It can be shown that the uniform circular array configuration is the only planar array geometry for which both $|\underline{\text{R}}(\theta)|$ and $|\underline{\widetilde{\text{R}}}^{\,2}(\theta)|$ are independent of θ. This implies that, in the case of a circular array, all the performance criteria investigated herein exhibit no dependence on azimuth θ. Such a geometry seems to be the obvious choice for applications where uniform performance at all azimuths is a necessity.

Y-shaped and X-shaped Arrays

Both Y-shaped and X-shaped arrays have a balanced-symmetric[3] geometry [3] and consequently their detection thresholds $(\text{SNR} \times L)_{det,\theta}$ are independent of θ. On the other hand both $(\text{SNR} \times L)_{res,\theta}$ and CRB_θ vary periodically as a function of θ with a period of 60° for the Y-array and of 90° for the X-array. Note that the best performance of the Y and X arrays occurs at even multiples of 30° and 45° respectively with worst performance occurring at odd multiples of 30° and 45° respectively.

L-shaped and CROSS-shaped Arrays

These two geometries are not balanced-symmetric and so the detection thresholds $(\text{SNR} \times L)_{det,\theta}$, exhibit significant variations with best performance at 45° and worst performance at 135° for the L-array and at 0°/180° and 90° respectively for the CROSS-array. Note also that the resolution threshold $(\text{SNR} \times L)_{res,\theta}$ and CRB_θ indicate best and worst performances at similar azimuths.

Dual-Ring Array

[3] Balanced symmetric array: $\underline{r}_x^T \underline{r}_y = 0$ and $|\underline{r}_x| = |\underline{r}_y|$

The dual-ring array is approximately balanced-symmetric and also resembles a circular-type structure. Consequently an almost uniform performance is provided at all azimuths. The detection $(\text{SNR} \times L)_{det,\theta}$ indicates best performance at 77° and worst performance at 167° while the resolution threshold function $(\text{SNR} \times L)_{res,\theta}$ and CRB_θ indicate best and worst performances at 68° and 126° respectively.

Dual-Spiral Array

The dual-spiral array is an example of an array geometry which has sensors clearly distributed in one predominant direction and so it is easier to observe the variations of $|\underline{\text{R}}(\theta)|$ as a function of θ. The detection $(\text{SNR} \times L)_{det,\theta}$ indicates best performance at 153° and worst performance at 63° while both $(\text{SNR} \times L)_{res,\theta}$ and CRB_θ indicate best and worst performances at 162° and 54° respectively.

A comparison of the array structures reveals that at, and only at, θ=90° (broadside) the linear array has the best performance but that there is a monotonic degradation in performance as emitters approach the end-fire position. In terms of average performance over all azimuths, the X-shaped array out-performs the others with the Y-shaped array taking second position. The worst performance is obtained with the dual-ring array which clearly suffers due to its small dimensions.

5. PERFORMANCE COMPARISON AND ARRAY NORMALISATION

It is well known that the aperture of an array (i.e. the maximum separation between any two sensors), plays an important role in the ability of an array to resolve two sources close together. Therefore it may be argued that, in order to perform a fair comparison, the DF capabilities should be investigated with the array geometries normalised with respect to aperture. In order to perform such a comparison the exercise of Section-4 is repeated with the sensor locations scaled such that each array has the same aperture of 57.918 half-wavelengths.

From the results shown in Figures 7-9, it is apparent that now the circular array exhibits the best performance which is independent of azimuth. The performance of the linear array approaches that of the circular array only at θ=90° (broadside) but rapidly shows a degradation as emitters approach the end-fire position. In terms of performance averaged over all azimuths, the X-shaped array and the Y-shaped array take the second position. The worst performance is obtained with the dual-spiral array.

As expected the variations of array performance with azimuth remain unchanged, apart from a scaling factor, when compared to the unnormalised case. This is because all array shapes are preserved through the normalisation process. The absolute performances of all the arrays are slightly improved as a result of an increase in array dimensions.

It is known that the resolution is also influenced by the length of the manifold curve (the longer the manifold curve the better the resolution). For a given aperture the length of the manifold curve is a function of the number of sensors. Therefore it may also be argued that a fairer performance comparison would be achieved with arrays normalised with respect to both aperture and number of sensors. In Figures 10-12 the results of this normalisation are shown with all array geometries having 24 elements. The normalisation was not possible for the dual ring and the dual spiral arrays, due to insufficient information regarding the rules defining their original sensor locations.

An important feature of an array geometry is its ability to provide a uniform DF performance over all azimuth directions. This property can be quantified by the following differential comparison rule

$$\textbf{\textit{differential}}(\text{SNR} \times L) = \mathbf{dB}\{(\text{SNR} \times L)_{best}\} - \mathbf{dB}\{(\text{SNR} \times L)_{worst}\}$$

where small $\textbf{\textit{differential}}(\text{SNR} \times L)$ corresponds to more consistent performance and therefore to a better array geometry.

In order to demonstrate the significance of this differential rule, it has been used to compare the original array geometries as well as their two normalised counterparts. The results are shown in Figure 13 in a bar-chart format. It is clear from this bar-chart that the difference is not affected by the normalisation and is a function only of the array geometry itself. Thus, using the above differential rule the array geometries may be ordered as shown in Table 3.

Table 3: Arrays order with respect to difference between best and worst performance

detection threshold				resolution threshold			
array	unnormalised	normalised		array	unnormalised	normalised	
		aperture	*aperture, N*			*aperture*	*aperture, N*
Circular	1st	1st	1st	Circular	1st	1st	1st
Y	1st	1st	1st	Dual Ring	2nd	2nd	–
X	1st	1st	1st	Y	3rd	3rd	2nd
Dual Ring	2nd	2nd	–	X	4th	4th	3rd
Dual Spiral	3rd	3rd	–	L	5th	5th	4th
Cross	4th	4th	2nd	Dual Spiral	6th	6th	–
L	5th	5th	3rd	Cross	7th	6th	5th
Linear	6th	6th	4th	Linear	8th	7th	6th

6. CONCLUSIONS

In this paper the ultimate direction-finding capabilities of a number of planar arrays have been investigated and compared. Criteria relating to the DF performance in terms of the minimum achievable bearing estimation error, and the detection and resolution thresholds have been determined using differential geometry properties of the array manifold.

The arrays were initially unnormalised and then normalised with respect to aperture and with respect to aperture and number of sensors. From the results it was concluded that the difference between the best and the worst detection and resolution performance is independent of the normalisation procedure being employed and is a characteristic only of the array geometry itself. However this should not be confused with the absolute performance of an array which is, of course, a function of both aperture and number of sensors.

A comprehensive set of results has been presented indicating the theoretical limits on accuracy, detection and resolution thresholds.

Thus these limits can be used as figures of merit to provide the performance level against which any existing or new algorithm can be compared. That is, for a given array, the closer a DF algorithm comes, performance-wise, to these theoretical limits the better.

REFERENCES

[1] DACOS, I., MANIKAS, A.: 'Estimating the Manifold Parameters of a One-Dimensional Array of Sensors,' *Journal of the Franklin Institute, Engineering and Applied Mathematics*, 1995, **332B**, (3), pp. 307-332

[2] MANIKAS, A, DACOS, I.: 'Investigating the Manifold Parameters of a Non Linear Array of Omnidirectional Sensors. Part II: Specialization to Planar Arrays of Arbitrary Geometry.' Unclassified-Research Report: AM-91-5, Department of Electrical and Electronic Engineering, Imperial College London, 1991

[3] KARIMI, H.R., MANIKAS A.: 'The Manifold of a Planar Array and its Effects on the Accuracy of Direction-Finding Systems,' *IEE Proc.- Radar, Sonar Navig.*, 1996, **143**, (6), pp. 349-357

[4] MANIKAS, A., KARIMI, H.R., DACOS, I.: 'Study of the Detection and Resolution Capabilities of One-Dimensional Array of Sensors by using Differential Geometry,' *IEE Proc.-Radar, Sonar Navig.*, 1994, **141**, (2), pp. 83-92

[5] STOICA, P., NEHORAI, A.: 'MuSIC, Maximum Likelihood and Cramér-Rao Bound,' *IEEE Trans. Acoust. Speech and Signal Process.*, 1989, **37**, (52), pp. 720-741

[6] SCHMIDT, R.O.: 'Multiple Emitter Location and Signal Parameter Estimation,' *IEEE Trans. Antennas Propag.*, 1986, **34**, (3), pp. 276-280

[7] GUGGENHEIMER, H.W.: 'Differential Geometry' (McGraw-Hill, 1973)

[8] LIPSCHUTZ, M.M.: 'Differential Geometry' (McGraw-Hill, 1969)

[9] VAN TREES, H.L.: 'Detection, Estimation and Modulation Theory-Part I' (John Wiley and Sons, 1968)

CAPTIONS

Figure 1

Variations in parameter estimation performance as a function of azimuth θ

(Phase reference is assumed to be at the array centroid.)

Figure 2

Monopole gain pattern

Figure 3

ARRAY STRUCTURES FOR STUDY

Figure 4

Detection Threshold (SNR $\times$ L) as a function of azimuth angle for two equi-powered emitters separated by $\Delta\theta$=0.5° about θ. (ϕ=30°)

Figure 5

Resolution Threshold (SNR $\times$ L) as a function of azimuth angle for two equi-powered emitters separated by $\Delta\theta$=0.5° about θ. (ϕ=30°)

Figure 6

Error standard deviation $\sqrt{\text{CRB}_\theta}$ as a function of azimuth angle for two uncorrelated emitters separated by $\Delta\theta$=0.5° about θ.

L=100, SNR=20dB, ϕ=30°

Figure 7

Detection Threshold (SNR $\times$ L) as a function of azimuth angle for two equi-powered emitters separated by $\Delta\theta$=0.5° about θ. (ϕ=30°)

The array geometries have been normalised with respect to aperture.

Figure 8

Resolution Threshold (SNR $\times$ L) as a function of azimuth angle for two equi-powered emitters separated by $\Delta\theta$=0.5° about θ. (ϕ=30°)

The array geometries have been normalised with respect to aperture.

Figure 9

Error standard deviation $\sqrt{\text{CRB}_\theta}$ as a function of azimuth angle for two uncorrelated emitters separated by $\Delta\theta$=0.5° about θ. (L=100, SNR=20dB, ϕ=30°)

The array geometries have been normalised with respect to aperture.

Figure 10

Detection Threshold (SNR $\times$ L) as a function of azimuth angle for two equi-powered emitters separated by $\Delta\theta$=0.5° about θ. (ϕ=30°)

The arrays have been normalised with respect to aperture and number of sensors.

Figure 11

Resolution Threshold (SNR $\times$ L) as a function of azimuth angle for two equi-powered emitters separated by $\Delta\theta$=0.5° about θ. (ϕ=30°)

The arrays have been normalised with respect to aperture and number of sensors.

Figure 12

Error standard deviation $\sqrt{\text{CRB}_\theta}$ as a function of azimuth angle for two uncorrelated emitters separated by $\Delta\theta$=0.5° about θ. (L=100, SNR=20dB, ϕ=30°)

The arrays have been normalised with respect to aperture and number of sensors.

Figure 13

Difference between best and worst detection and resolution thresholds performance for unnormalised and normalised array structures

$|\underline{R}(\theta)|$ = large ⇒ ϕ-estimation=GOOD
$|\underline{R}(\theta+90°)|$ = small ⇒ θ-estimation=POOR

$|\underline{R}(\theta)|$ = small ⇒ ϕ-estimation=POOR
$|\underline{R}(\theta+90°)|$ = large ⇒ θ-estimation=GOOD

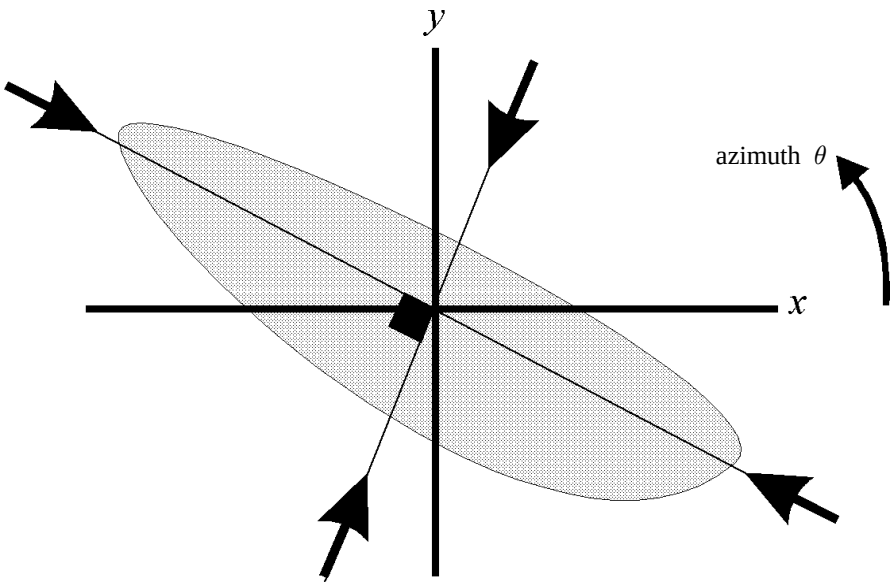

Figure 1

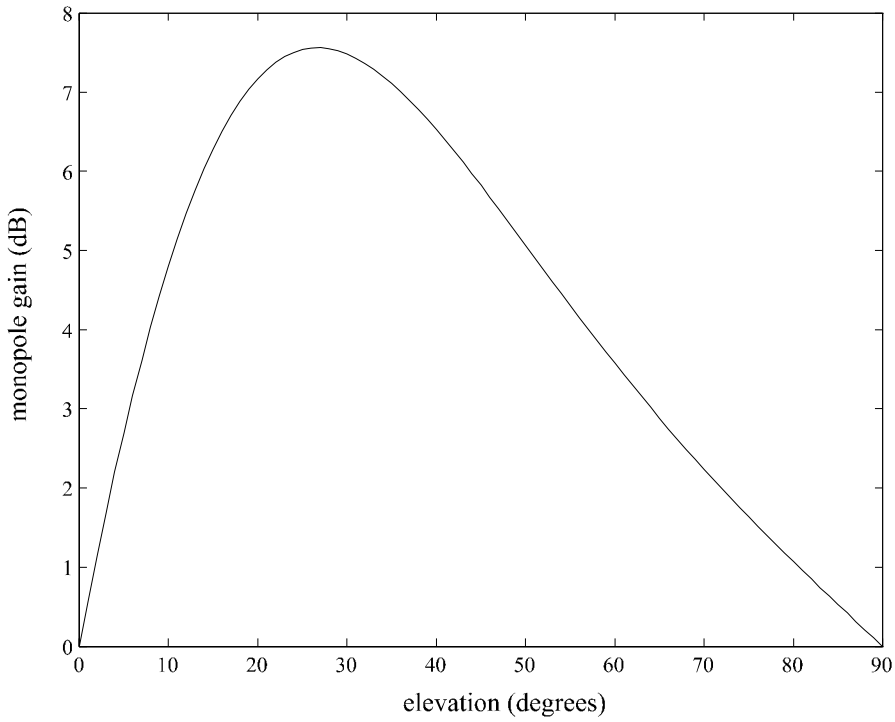
monopole gain (dB)
elevation (degrees)
0
1
2
3
4
5
6
7
8
0
10
20
30
40
50
60
70
80
90

Figure 2

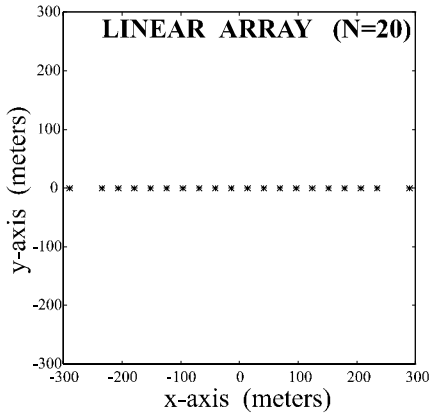
LINEAR ARRAY (N=20)
y-axis (meters)
x-axis (meters)

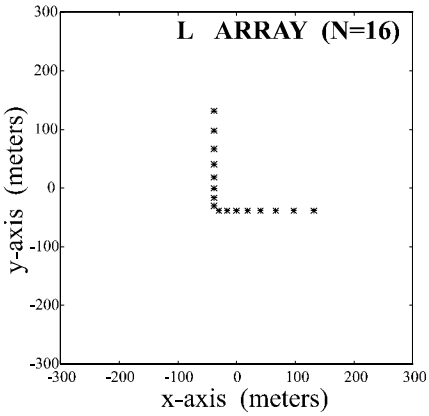
L ARRAY (N=16)
y-axis (meters)
x-axis (meters)

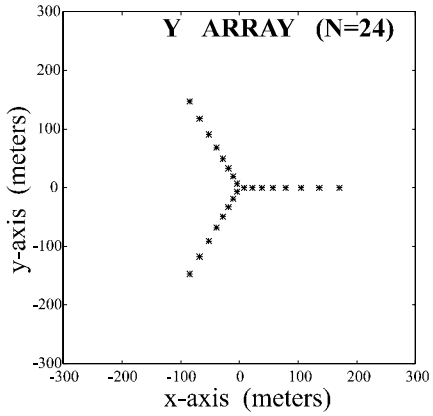
Y ARRAY (N=24)
y-axis (meters)
x-axis (meters)

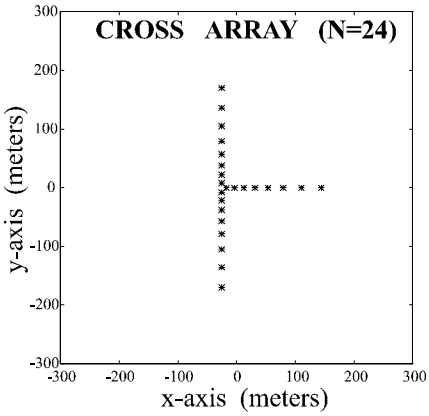
CROSS ARRAY (N=24)
y-axis (meters)
x-axis (meters)

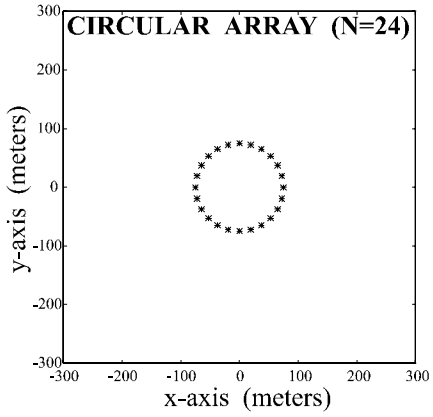
CIRCULAR ARRAY (N=24)
y-axis (meters)
x-axis (meters)

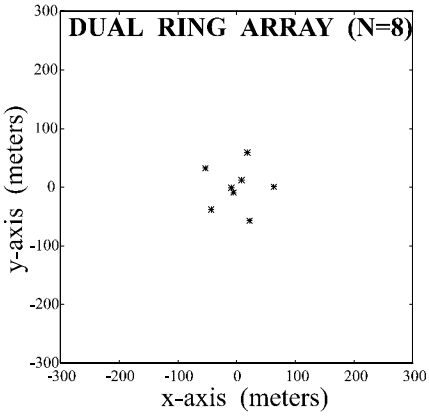
DUAL RING ARRAY (N=8)
y-axis (meters)
x-axis (meters)

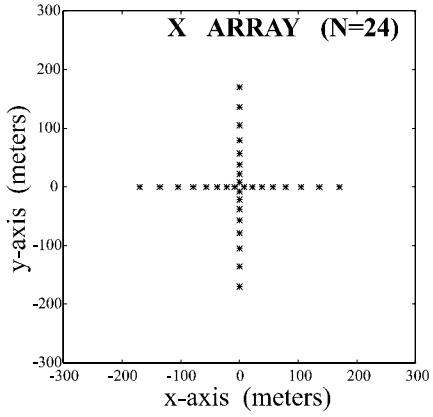
X ARRAY (N=24)
y-axis (meters)
x-axis (meters)

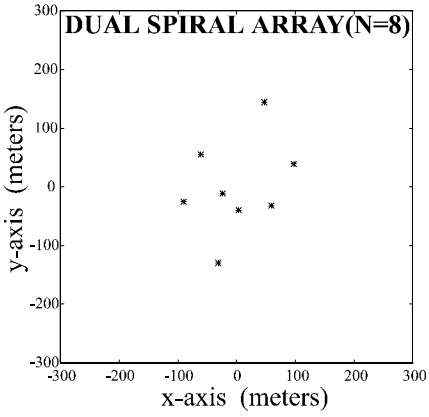
DUAL SPIRAL ARRAY(N=8)
y-axis (meters)
x-axis (meters)

Figure 3

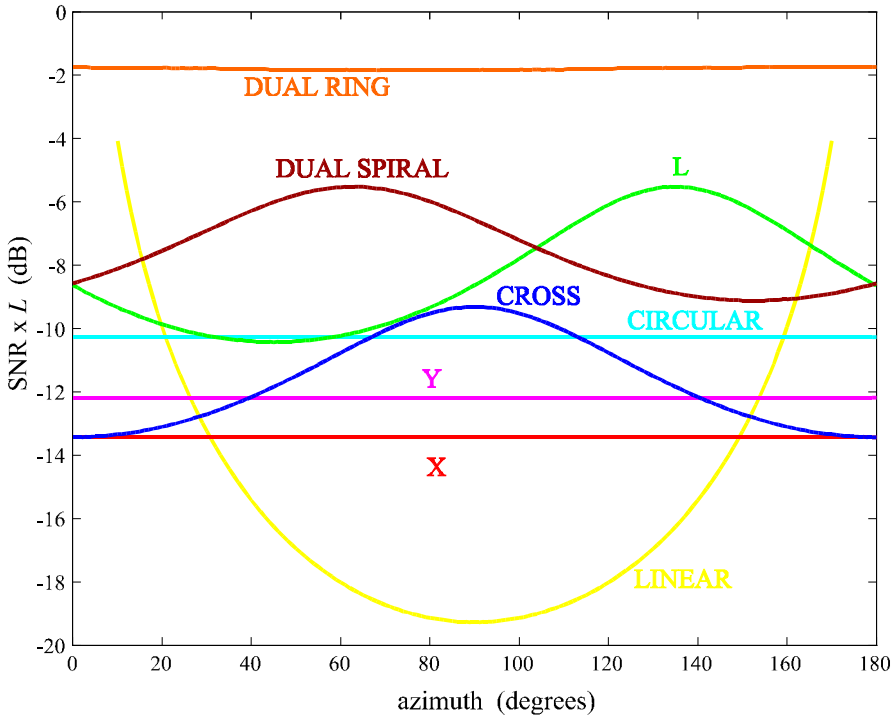
DUAL RING
DUAL SPIRAL
L
CROSS
CIRCULAR
Y
X
LINEAR
SNR x L (dB)
azimuth (degrees)
0
-2
-4
-6
-8
-10
-12
-14
-16
-18
-20
0
20
40
60
80
100
120
140
160
180

Figure 4

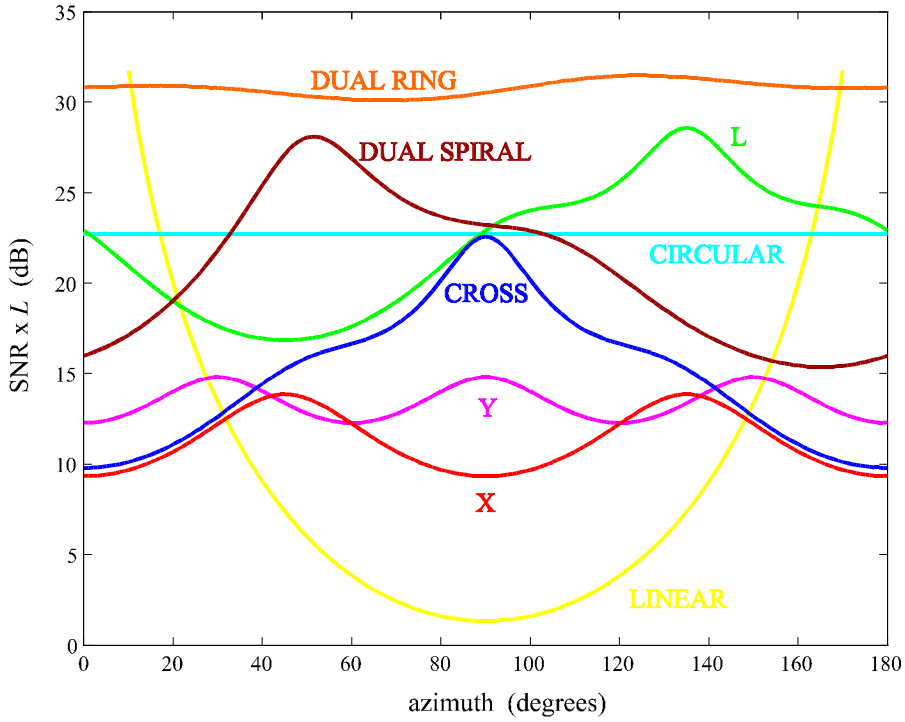
DUAL RING
DUAL SPIRAL
L
CIRCULAR
CROSS
Y
X
LINEAR
SNR x L (dB)
azimuth (degrees)
0
5
10
15
20
25
30
35
0
20
40
60
80
100
120
140
160
180

Figure 5

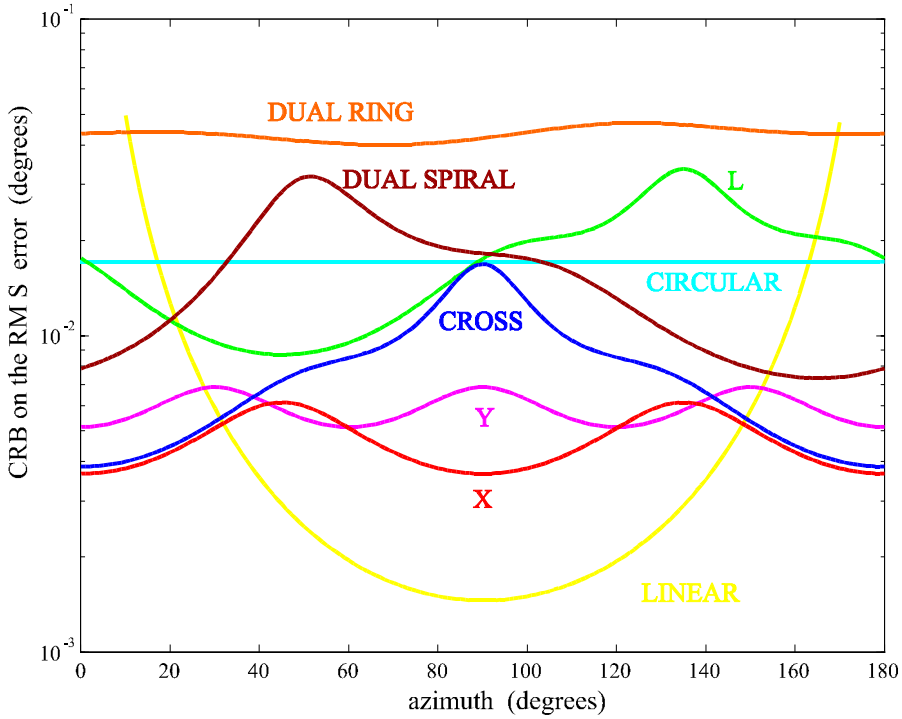
DUAL RING
DUAL SPIRAL
L
CIRCULAR
CROSS
Y
X
LINEAR
CRB on the RM S error (degrees)
azimuth (degrees)
10^-1
10^-2
10^-3
0
20
40
60
80
100
120
140
160
180

Figure 6

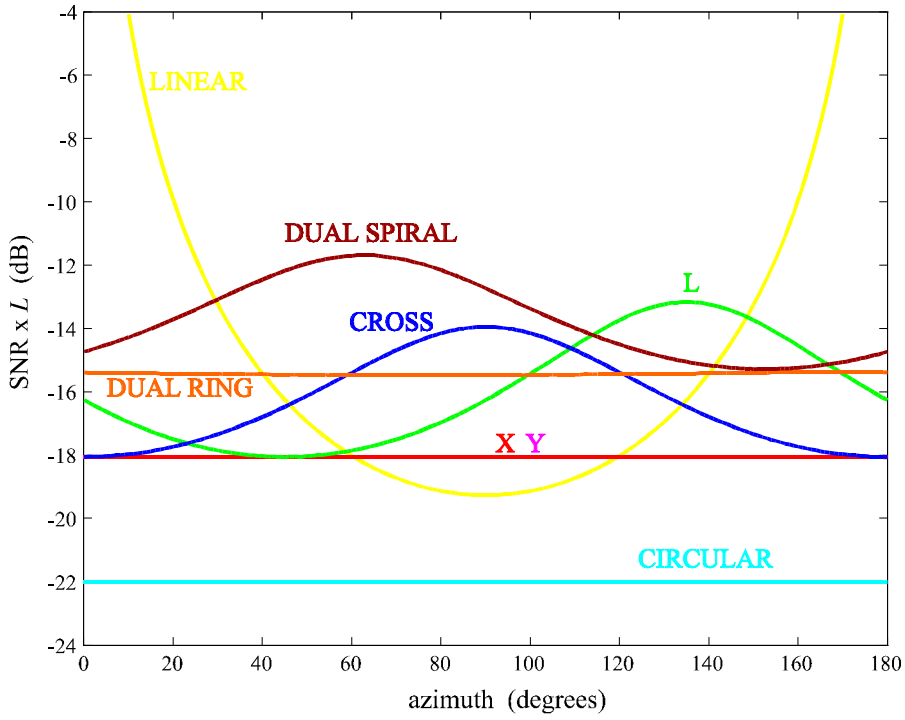
LINEAR
DUAL SPIRAL
L
CROSS
DUAL RING
X Y
CIRCULAR
SNR x L (dB)
azimuth (degrees)
-4
-6
-8
-10
-12
-14
-16
-18
-20
-22
-24
0
20
40
60
80
100
120
140
160
180

Figure 7

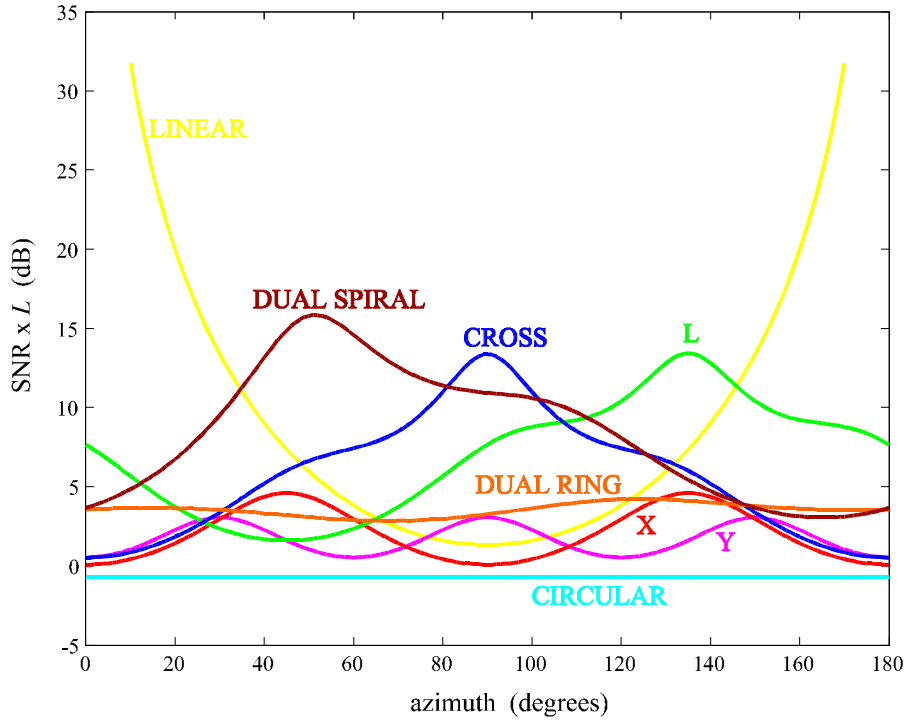
LINEAR
DUAL SPIRAL
CROSS
L
DUAL RING
X
Y
CIRCULAR
SNR x L (dB)
azimuth (degrees)
35
30
25
20
15
10
5
0
-5
0
20
40
60
80
100
120
140
160
180

Figure 8

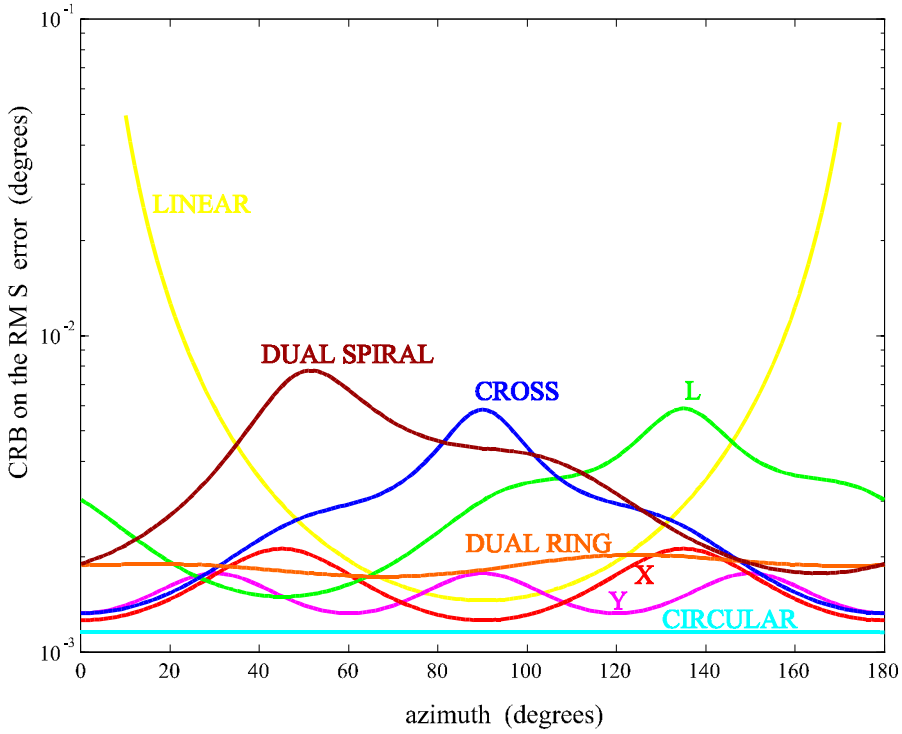
CRB on the RM S error (degrees)
azimuth (degrees)
LINEAR
DUAL SPIRAL
CROSS
L
DUAL RING
X
Y
CIRCULAR

Figure 9

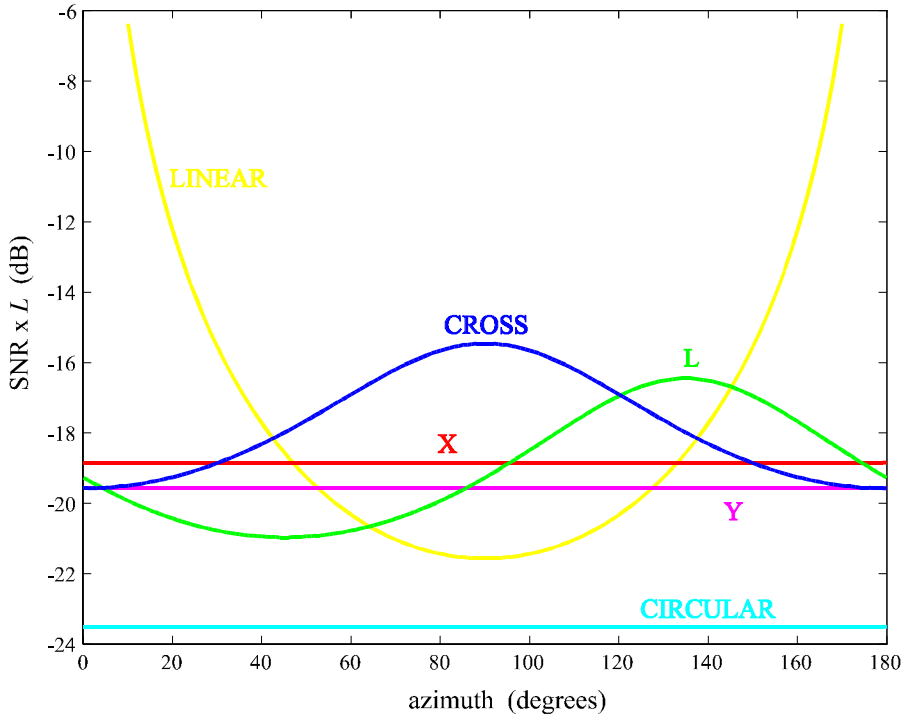
-6
-8
-10
-12
-14
-16
-18
-20
-22
-24
SNR x L (dB)
0
20
40
60
80
100
120
140
160
180
azimuth (degrees)
LINEAR
CROSS
L
X
Y
CIRCULAR

Figure 10

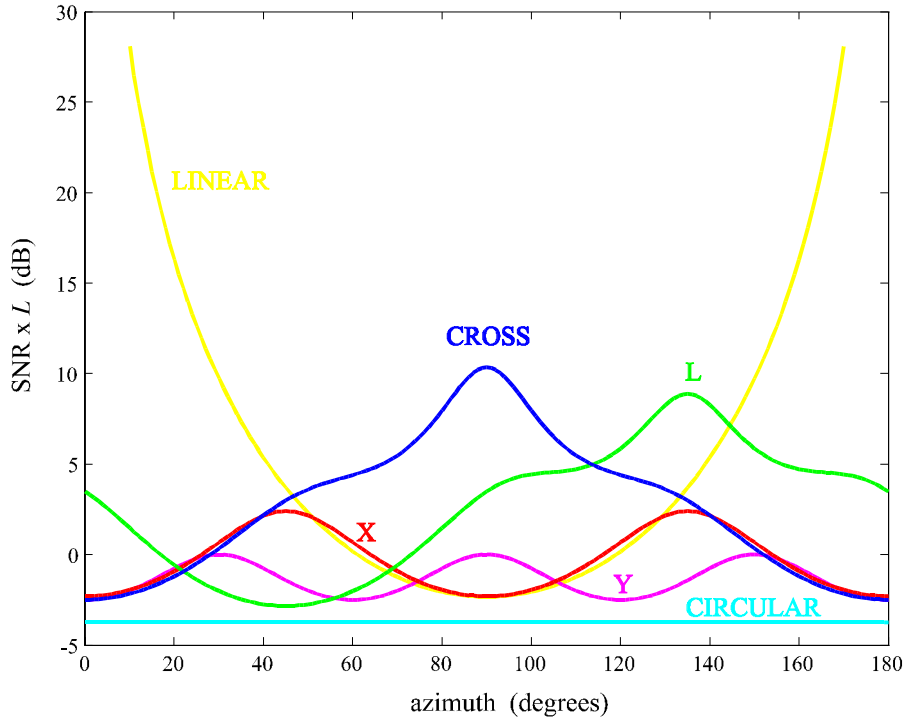
LINEAR
CROSS
L
X
Y
CIRCULAR
SNR x L (dB)
azimuth (degrees)
30
25
20
15
10
5
0
-5
0
20
40
60
80
100
120
140
160
180

Figure 11

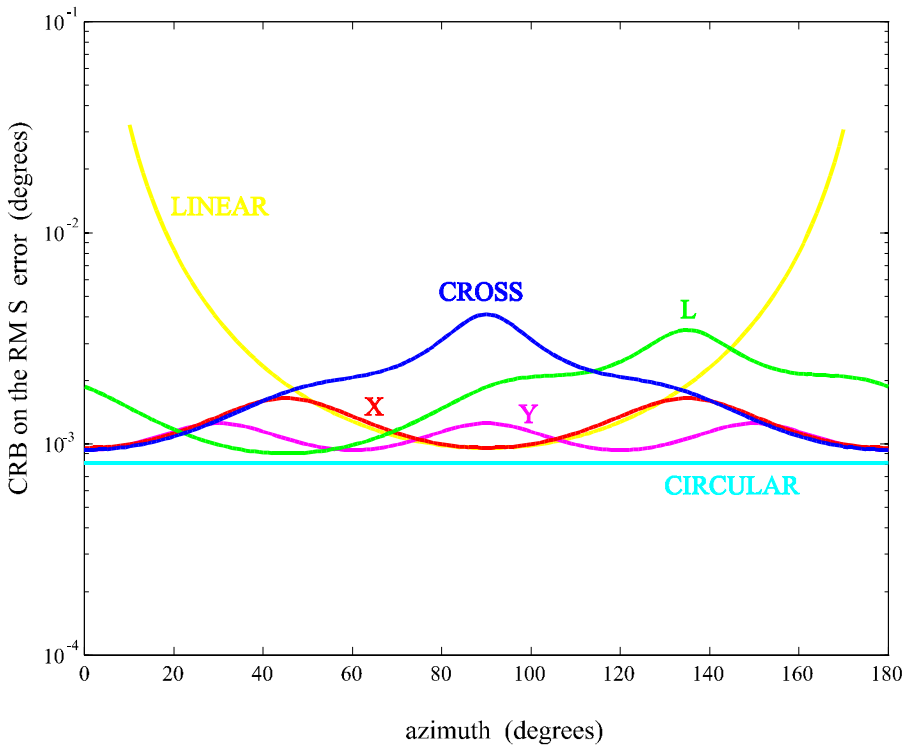
CRB on the RM S error (degrees)
azimuth (degrees)
LINEAR
CROSS
L
X
Y
CIRCULAR
10^-1
10^-2
10^-3
10^-4
0
20
40
60
80
100
120
140
160
180

Figure 12

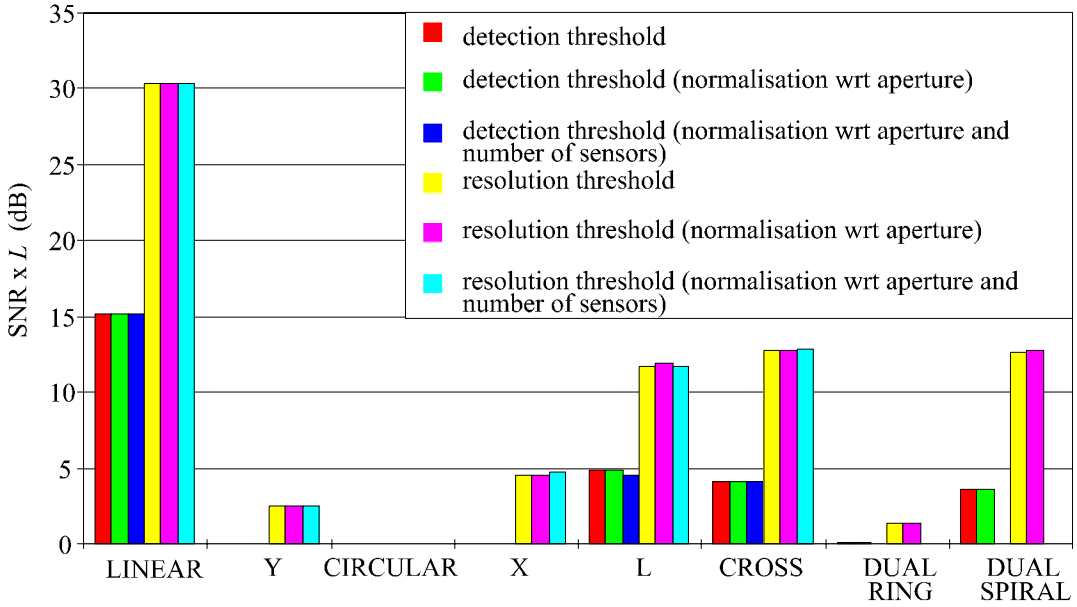
35
30
25
20
15
10
5
0
SNR x L (dB)
detection threshold
detection threshold (normalisation wrt aperture)
detection threshold (normalisation wrt aperture and number of sensors)
resolution threshold
resolution threshold (normalisation wrt aperture)
resolution threshold (normalisation wrt aperture and number of sensors)
LINEAR
Y
CIRCULAR
X
L
CROSS
DUAL RING
DUAL SPIRAL

Figure 13